Palaeogeography, Palaeoclimatology, Palaeoecology 680 (2025) 113362

Contents lists available at ScienceDirect

Palaeogeography, Palaeoclimatology, Palaeoecology

journal homepage: www.elsevier.com/locate/palaeo

Late-Holocene compound flood events in southern China: Geochemical evidence and global climatic linkages

Muyi Zhang [a], Zixian Zhuang [b], Zhaoquan Huang [a], Nannan Li [c], Jianghui Li [a], Shengtao Liu [d], Fengling Yu [a,*]

[a] *Department of Geological Oceanography, State Key Laboratory of Marine Environmental Science, College of Ocean and Earth Sciences, Xiamen University, Xiamen 361102, China*
[b] *Xiangcheng District People's Government, Zhangzhou 363000, China*
[c] *ICARUS, Department of Geography, Maynooth University, Maynooth, Co., Kildare, W23 F2H6, Ireland*
[d] *Jiangxi Water Investment Construction Group Co., Ltd, Nanchang 330006, China*

ARTICLE INFO

Editor: P Srivastava

Keywords:
Compound flood
Typhoon
Geochemical records
Global warming
Sea level change

ABSTRACT

Compound flood poses great threats to both coastal environments and human societies. To improve understanding of the sedimentary characteristics and underlying mechanisms of palaeo-compound floods in subtropical region, this study was conducted at the Zhangjiang Estuary, southern China, a site that frequently suffered from mega-typhoon hazards. In this study, sediment grain size, bulk organic $\delta^{13}C$, C/N, and major and trace elements using an XRF core scanner were analyzed for a percussion core taken from the estuary. AMS ^{14}C dating indicates that the core spans approximately 4300–500 cal. yr BP, with an average sedimentation rate of 0.21–1.94 mm/yr. Grain size analysis helps identify at least six major compound flooding events from the core that is predominantly composed of silt and clay sediment (50–75 %), interspersed with frequent sandy depositional layers where sand content ranges from 25 % to 50 %. The combined grain size and the elemental and isotopic signature from these sandy deposits suggest these sandy layers may come from a mix of fluvial/terrestrial and coastal/marine sources. Therefore, these sandy depositional sediments represent compound flooding events, a result from both fluvial flooding and storm surges, rather than being attributed to solely storm surges or fluvial flooding. Furthermore, typhoons could be the primary driving mechanisms for the compound flood events identified in this study. Because typhoons tend to produce severe rainfall-driven fluvial floods and strong wind-driven storm surges. This explanation is further supported by the similar recurrence period of 400–700 years between compound floods and severe typhoon activities in the region, and their occurrence times are highly synchronized. This study provides a detailed record of typhoon-induced compound flooding and offers insights into their sedimentary features and periodicity. Findings of this study are crucial for risk assessment and mitigation strategies in subtropical coastal regions under the background of global warming.

1. Introduction

As global warming intensifies, coastal compound floods have become an important disaster threatening coastal cities and low-lying coastal areas (Zscheischler et al., 2018). A coastal compound flood is a type of flooding event that occurs in coastal regions as a result of the interaction and combined effects of multiple hazards, such as storm surges, high tides, heavy precipitation, and high riverine discharge (Chan et al., 2024; Green et al., 2025). Coastal compound floods have resulted in much more serious disasters than floods caused by a single factor (Wahl et al., 2015; Aziz et al., 2024), which urges the necessity of investigating the characteristics of coastal disasters. Geological records are characterized by their long temporal coverage and the comprehensive preservation of information, offering a valuable archive for understanding the characteristics of historical coastal compound flooding hazards (Yu and Switzer, 2014; Benito et al., 2023).

Previous studies have extensively examined sandy deposits on coral reefs, beach ridges, and back-barrier lagoons to reconstruct past tropical cyclone activity (Zhou et al., 2021), and focused on tempested deposits characterized by hummocky cross-stratification and flume-experiment

---

* Corresponding author.
E-mail address: fengling.yu@xmu.edu.cn (F. Yu).

https://doi.org/10.1016/j.palaeo.2025.113362
Received 27 July 2025; Received in revised form 17 October 2025; Accepted 17 October 2025

analogues to investigate palaeo-storms (Yu et al., 2013; He et al., 2023). However, while the combined sedimentary signature of simultaneous surge and landward flooding remains poorly constrained. For instance, studies have revealed that storm surge–induced sediment pulses can exceed overbank fluvial inputs—as demonstrated by hurricane-driven accretion in the Mississippi Delta, where Turner et al. (2006) estimated storm surge delivered 131 × 10^6 MT of sediment, about 5.5 times more than annual riverine inputs.

Recognizing how severe coastal compound flooding events can pose disproportionate hazards to coastal–estuarine systems, sedimentological research has largely focused on how to distinguish between storm-driven (marine) and rainfall/river-driven (terrestrial) deposits through a variety of proxies (Green et al., 2025). In addition, geochemical tracers (e.g., Sr and Li isotopes) and stable isotopes ($\delta^{18}O$, $\delta^{13}C$) have been successfully applied to differentiate marine, terrestrial, and freshwater sources, and grain-size end-member modelling has helped reconstruct flood energy and inundation pathways (Peng et al., 2019). Compound floods usually generate complex sedimentary records that are distinct from those produced by individual flood drivers. Compound flooding deposits usually archive multiple sources of sediment after multiple flood drivers within a single event.

In global paleoflood research, subtropical coastal zones have emerged as critical areas due to their high population density, economic significance, and frequent exposure to cyclonic activity (Lee et al., 2012; Zemunik et al., 2022). However, the interpretation of high-energy event records preserved in the estuarine deposits of these regions remains challenging. A central difficulty is that the sedimentary records of compound flood events, which are by definition driven by concurrent forces, are often simplistically attributed to a single driver, such as a storm surge or a fluvial flood (Chiverrell et al., 2019). This oversimplification often stems from a reliance on single proxies, as an individual indicator may only capture the most dominant signal of a multifaceted event (Shi et al., 2015; Wei et al., 2019). Therefore, it is crucial to employ a multi-proxy approach, integrating geochemical data with other sedimentological (e.g., grain size, microfossils) and historical evidence to gain a better understanding of past compound flooding events (Switzer et al., 2014; Razum et al., 2020; Szcześniak et al., 2023; Smrkulj et al., 2025), which will provide information of the timing, magnitude, and interaction of the different driving factors (Yang et al., 2023; Wang et al., 2024; Ali et al., 2025).

Tropical and subtropical coasts are particularly vulnerable to compound floods due to their dense populations, economic importance, and the frequent occurrence of typhoons or hurricanes (Khan et al., 2013; Zemunik et al., 2022). Aiming to improve our understanding of paleo–compound flood along subtropical coasts, this study applies multiple proxies to reconstruct the history of such events using a case study from southern China. To achieve this, we pursue three main objectives including, 1) defining the sedimentary feature of compound flooding events, 2) examining the driving mechanism of the compound floods, and 3) exploring the late-Holocene compound floods in the subtropical region and its implications for future coastal flooding. The findings of this study will deepen our understanding of the characteristics of coastal compound floods in the subtropical area and provide clues for understanding their possible future trends and impacts.

2. Regional setting

Fujian Province at the southeastern China (Fig. 1A) is a predominantly mountainous region, with upland areas in the west accounting for about 80 % of the total land area. In contrast, the coastal plain in the east is relatively narrow, where several small rivers flow into the sea (Fu et al., 2020; Wei et al., 2023). The Fujian coast is a region frequently affected by tropical cyclones or typhoons in China, and it receives a much higher frequency of typhoons landfalls than the Yangtze River Delta region (Yin et al., 2010; Lee et al., 2012). Between 1945 and 2014, more than 120 subtropical cyclones made landfall along the Fujian coast This number could be approximately doubled if cyclones impacting Fujian Province but making their landfall outside the region were also included (Wei, 2019). Official data indicate substantial economic losses caused by coastal hazards (Fujian Provincial Marine Disaster Bulletin, 2023). In 2023, a total of four typhoons with severe storm surges occurred along the Fujian coast, causing direct economic losses of

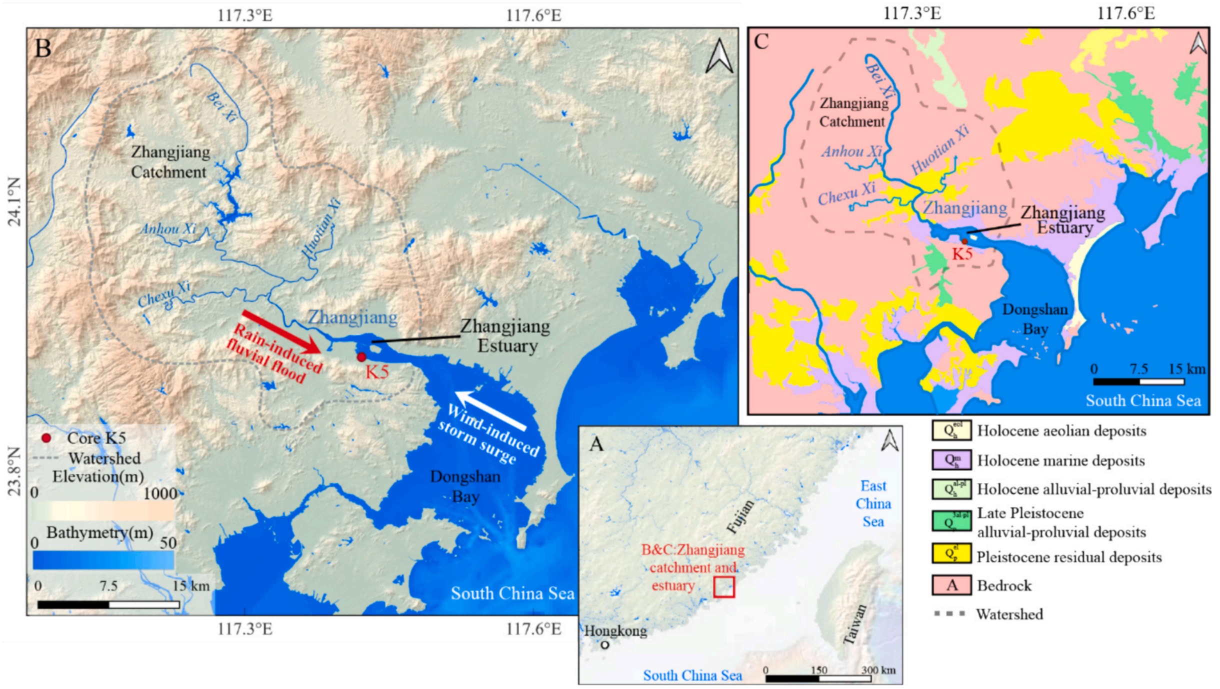

Fig. 1. Study area. A: Geographical location of the study area; B: Location of Core K5 and the hydraulic condition. C: Geological map of the study area, showing the distribution of Quaternary sediment at the lower catchment. Map modified from the "Geological map of Fujian coastal zone" provided by the Nanjing Center of Geological Survey via the GeoCloud (https://geocloud.cgs.gov.cn/).

around 2 billion RMB (about 28 million USD). From 2019 to 2023, marine disasters caused a direct economic loss of about 2.4 billion RMB (around 34 million USD) to the province. About one in six typhoons that make landfall in the Fujian coast have affected the estuary under this study. Furthermore, the tide gauge station in Dongshan at the mouth of the estuary has exceeded the alert tide level 32 times between 1959 and 2015 (Fang et al., 2017; Wei, 2019).

Zhangjiang River in the southern part of the Fujian Province, China, has a total length of 66.2 km, a watershed area of 1038 km^2, an average annual discharge of 1.01×10^9 m^3 and a sediment flux of 0.04×10^4 t/km^2 (Li et al., 2018). Zhangjiang River is a mountainous river under the subtropical monsoon climate, and its catchment is characterized with steep valley and high aspect ratio, which is particularly susceptible to severe soil erosion during strong summer rainfall. Zhangjiang Estuary (Fig. 1B), has a mean tidal range of approximately 2 m, and its maximum reaches about 3 m. Within the estuary, there is the Zhangjiang Mangrove National Nature Reserve, covering an area of 23.6 km^2, where the mangrove forests and Spartina grow. Dongshan Bay is a typical semi-enclosed marine bay connecting the Zhangjiang Estuary and the sea. Dongshan Bay receives sediments primarily from the Zhangjiang River, surrounding coast and the sea (Fig. 1C; Gao et al., 2021).

3. Methods and materials

3.1. Core collection and pretreatments

In May 2018, the percussion core K5 (23°55′15.87″N, 117°24′57.82″E), was collected from the margin of the Zhangjiang Mangrove National Nature Reserve at the base of an adjacent mountain (Fig. 1). The core had a total recovery of 554 cm, with the uppermost 89 cm consisting of artificial landfill (primarily construction waste), which was underlain by 214 cm of natural deposits (90–303 cm) overlying weathered bedrock. This study focuses exclusively on the natural sediment section from 90 to 303 cm. For the purposes of analysis, the top of this section (90 cm) is designated as the 0 cm reference depth.

Core K5 was split longitudinally into a working half and an archive half. The working half was visually logged, photographed, and then scanned with an XRF core scanner to determine elemental concentrations. Following the non-destructive scanning, the core was subsampled at 1 cm or 3 cm intervals depending on lithological changes, yielding a total of 193 subsamples. These subsamples were subsequently prepared for grain size and bulk organic carbon isotopic analyses.

3.2. Sample analyses

3.2.1. AMS ^{14}C dating

Selected materials, including plant fragments, foraminifera and bulk sediment sample, were prepared for AMS ^{14}C dating (Table 1). Results were calibrated into calendar years before the present (BP, 1950 CE), using the Calib 8.20 software: The IntCal20 curve was used for the age calibration of terrestrial samples, while the Marine20 curve was used for the age calibration of marine samples (Reimer et al., 2013). For the marine samples, a local marine reservoir correction (ΔR) of -66 ± 30 years was applied during calibration, based on the Marine Reservoir Correction Database (Marine Reservoir Correction Database, http://calib.org/marine/). The final age-depth model was constructed using the Bchron R package (Haslett and Parnell, 2008; Parnell et al., 2008).

3.2.2. Relative elemental content analysis

The relative abundances of major elements in Core K5 were measured using an X-Ray Fluorescence (XRF) Core Scanner (AVAATECH 3RD) at a 2 mm interval and a voltage of 30 kV. All XRF scanning and analysis were performed at the Centre for Large-Scale Instrumentation and Technology Services, State Key Laboratory of Marine Environmental Science (MEL), Xiamen University.

Gaps exist in the elemental data for certain sections of the core due to two main reasons: Firstly, at the drill bit position, no XRF scan was performed due to severe sample deformation; And secondly, reliable data could not be obtained from layers with coarser grain sizes due to high porosity. In order to ensure the continuity and comparability of the data set and facilitate comparison with other indicators, this study adopted multiple methods to interpolate the layers with missing element data, and finally selected the most reasonable interpolation result for discussion. After selecting multiple interpolation methods and interpolation indicators, we finally used the average grain size linear interpolation as the reference for the interpolation result because of its high resolution, correlation and the method is in line with the actual interpolation situation. Finally, cluster analysis of the XRF scanning results was performed using PAST software (Hammer et al., 2001).

3.2.3. Grain size analysis

A total of 193 subsamples were prepared for grain size analysis following the pretreatment methods of Gao et al. (2021). For each analysis, approximately 2 g of wet sample was weighed, oven-dried for 12 h, and reweighed to determine its dry mass. The dried samples then underwent chemical treatment to remove organic matter with 20 % H_2O_2 and carbonates with 10 % HCl. To ensure complete particle disaggregation, the samples were subsequently soaked in a sodium hexametaphosphate solution for 12 h. The particle size distribution was then measured using a Malvern Mastersizer 3000 laser particle analyzer at the Department of Geological Oceanography, College of Ocean and Earth Sciences, Xiamen University. Following the analysis, grain size fractions were classified as clay, silt, and sand based on the Shepard classification scheme (Shepard, 1954; Gao et al., 2021). The environmentally sensitive grain-size component was identified by calculating the standard deviation of the grain-size distribution, following the method of Boulay et al. (2023).

3.2.4. Bulk organic stable organic carbon isotope analysis

Pretreatment of the bulk organic carbon isotope method followed the method of Yu et al. (2010). Approximately 1 g of dry sample was acidified with 10 ml of 1 mol/l HCl to remove carbonates, then rinsed three times with deionized water to neutralize the sample and freeze dried. The dried samples were then ground to 200 mesh using an agate mortar and pestle. About 50 mg of the ground sample was precisely weighed

Table 1
Results of AMS ^{14}C dating of Core K5.

Lab code	Sample label	Depth (cm)	Material	Conventional age (yr BP)	Calibrated age (cal. yr BP)
Beta-574,792	YXK5–17	**16**	Bulk sediment	1690 ± 30	1694–1534
Beta-566,738	YXK5–49	69	Plant debris	1010 ± 30	976–800
Beta-549,730	YXK5–82	102	Plant debris	1780 ± 30	1813–1616
Beta-546,030	YXK5–113	135	Foraminifera	3340 ± 30	3379–3154
Beta-553,924	YXK5–152	**172**	Plant debris	5660 ± 30	6503–6324
Beta-574,796	YXK5–160	**180**	Bulk sediment	5380 ± 30	6282–6021
Beta-564,677	YXK5–170	202	Plant debris	3790 ± 30	4285–4084

and sealed in a tin capsule for the analysis of the total organic carbon (TOC), total nitrogen (TN) and their isotopic compositions ($\delta^{13}C$) of the bulk sediment sample. Analyses were carried out using an elemental analyzer (Elementar Analysensysteme GmbH, Hanau, Germany) coupled with a PDZ Europa 20–20 isotope ratio mass spectrometer at the Stable Isotope Facility, University of California Davis, USA. The $\delta^{13}C$ values are reported relative to the international VPDB (Vienna Pee Dee Belemnite) standard, and results are expressed in parts per mil (‰). The long-term standard deviation for $\delta^{13}C$ is 0.2 ‰. The C/N molar ratio, defined as the ratio of TOC to TN, is referred to as the C/N ratios throughout the text (Yu et al., 2010).

3.3. *Semi-quantification of the provenance of compound flooding deposits*

Utilizing a sediment source end-member model analysis, we employed a Bayesian mixing model to quantify the relative contributions of land rivers and storm surges to compound floods (Phillips and Gregg, 2003). This method incorporates prior probability distributions of multiple input indicators and samples. By applying a Monte Carlo simulation with extensive repeated sampling, we estimated the contribution ratio parameters of the influencing factors within the Bayesian model (Gelman et al., 2013).

Assume there are n samples ($i = 1\ldots N$) whose contribution to the driving factor needs to be determined separately. Each sample has M tracer values (j = 1…M), and a total of T endmembers (influencing factors, k = 1…T). The prior probability of having endmembers is as follows

$$e_{kj} \sim N\left(\mu_{kj}\omega_{kj}^{2}\right) \tag{1}$$

$e_{jk}$is the trace value of an endmember, μ is the mean value of e_{jk}; and ω is the standard deviation of e_{jk};

And the endmember contribution rate of each sample:

$$p_i = (p_{i1},\ldots,p_{iK}) \sim Dirichlet(\alpha_1,\ldots,\alpha_K)\ i = 1,\ldots,N \tag{2}$$

The mix model as follows:

$$m_{ij} = \sum_{k=1}^{T} p_{ik}e_{kj} + \varepsilon_{ij}\ i = 1,\ldots,N, j = 1,\ldots,M \tag{3}$$

Observed data (assuming homogeneous measurement errors σ_{obs}):

$$\varepsilon_{ij} \sim N\left(0,\sigma_j^2\right) \tag{4}$$

$\varepsilon_{ij}$is the residual value of isotope j of sample i; the mean value of ε_{ij} is zero; and the σ is the standard deviation ε_{ij}.

Posterior distribution, according to the Bayesian formula, the joint posterior is

$$p\left(\{p_{ik}\},\{e_{kj}\}\mid\left\{y_{ij}\right\}\right) \propto \prod_{i=1}^{N}\prod_{j=1}^{M} N\left(y_{ij}\middle|\sum_{k} p_{ik}e_{kj},\sigma_{obs}^{2}\right) \times \prod_{i=1}^{N} Dir(\mathbf{p}_i|\boldsymbol{\alpha}) \times \prod_{k=1}^{T}\prod_{j=1}^{M} N\left(e_{kj}|\mu_{kj},\sigma_{kj}^{2}\right) \tag{5}$$

The Markov Chain Monte Carlo (MCMC) algorithm is used to draw samples from this posterior distribution to estimate the posterior distribution characteristics of each endmember contribution rate and endmember tracer value.

We implemented the calculation of this model using the python pyMC package (Salvatier et al., 2016).

The tracer values ($\delta^{13}C$ and C/N ratios) for the five end-members (Soil, C3 plants, C4 plants, Freshwater POM, and Marine POM) were established based on a comprehensive dataset of modern analogue samples collected from the Zhangjiang Estuary system, as detailed in Yu et al. (2025).

4. Results

4.1. *Chronological framework*

4.1.1. *AMS ^{14}C dating results*

The AMS ^{14}C dating results indicate that the ages generally align well with the stratigraphic sequence, except for two age reversals observed at the depths of 16 cm and 172–180 cm (Table 1). Common causes of age reversals include (Yu and Switzer, 2014): (a) biological activities, such as the penetration of younger plant roots into older strata or bioturbation; (b) geological processes, such as the inversion of strata due to intense geological and tectonic movements; and (c) sediment re-transportation caused by natural and/or anthropogenic processes, which relocates materials from the old strata into younger layers.

In this study, the age at 16 cm depth is older than that of the underlying strata. Given that the original 0–89 cm layer at the sampling site consists of artificial fill, it is highly likely that older material was introduced through human activities. Similarly, the older ages at 172–180 cm depth are most likely due to the transport of material from older strata by natural event (such as storm etc.) driven processes. This interpretation is supported by subsequent mathematical and statistical analyses in the age model (see Section 4.1.2) and by proxy analysis results (see Sessions 4.2–4.3).

4.1.2. *Age-depth model*

The age-depth model is constructed using the Bayesian statistical method, implemented through the R package Bchron (Heegaard et al., 2005; Haslett and Parnell, 2008; Parnell et al., 2008). The model first estimates the incremental probability distribution and identifies outliers, excluding the age reversals. It then builds the age-depth model based on a bivariate monotonic Poisson-gamma process with the selected dates. The final age-depth model is presented in Fig. 2.

The age model indicates that Core K5 spans approximately 4280 to 530 cal. yr BP, with an average sampling resolution of about 17.5 yrs./cm and a sedimentation rate ranging from 0.21 to 1.94 mm/yr, with an average of approximately 0.57 mm/yr. Overall, the deposition rate is relatively fast during 4280–3100 cal. yr BP at 0.71 mm/ yr, then slows

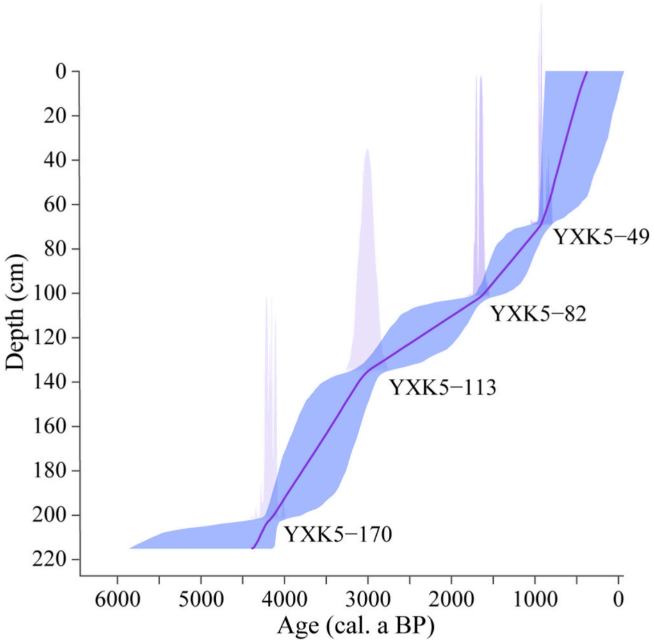

Fig. 2. Age-depth model of Core K5 with the 95 % confidence level represented by the shaded green area. The age model is developed via Bchron (Heegaard et al., 2005). (For interpretation of the references to colour in this figure legend, the reader is referred to the web version of this article.)

down during 3100–800 cal. yr BP at 0.30 mm/yr, and increases to 1.68 mm/yr after 750 cal. yr BP.

4.2. Grain size composition

For the sediments of Core K5, on average, the sand content is 12.08 %, silt content is 69.49 %, and clay content is 18.39 % (Fig. 3A). The most significant grain size fraction lies between 8 and 16 μm, comprising approximately 74 % of the total sediment content in Core K5.

The results of the sensitive grain size component analysis are presented in Fig. 3B. The dominant grain size fraction ranges from 1.7 to 31.1 μm, representing the primary silt fraction in the core. Coarser fractions (>31.1 μm) are primarily associated with extreme hydrological events, and the discussion below focuses on these changes. Based on grain size composition, layers with an average grain size >31.1 μm are classified as sandy depositional layers (S layers), indicating a higher sand proportion compared to the core average. The remaining layers are classified as normal deposit layers (N layers). Accordingly, Core K5 is divided into seven normal layers (N1 to N7) and six sandy layers (S1 to S6), as shown in Fig. 3A. Based on our age-depth model (Fig. 2), the approximate ages for these sandy depositional events are: S1 (740–710 cal. yr BP), S2 (1190–1020 cal. yr BP), S3 (1320–1280 cal. yr BP), S4 (2740–2600 cal. yr BP), S5 (3400–3320 cal. yr BP) and S6 (3830–3800 cal. yr BP), respectively.

Significant differences in particle size distribution between the N and S layers are shown (Fig. 3C). S1 Layer exhibits irregular trimodal and bimodal distributions, both characterized by broad main peaks ranging from 2 to 400 μm and low peak frequencies (~3 %). S2 and S5 Layers show bimodal distributions, with wider primary peaks (2–500 μm) and lower frequencies (< 4 %) compared to N layers. S3 Layer displays a unimodal distribution, with peaks ranging from 2 to 400 μm and frequencies above 5 %. S4 and S6 Layers exhibit trimodal distributions with distinct characteristics. The main peaks of S4 range from 2 to 100 μm, while those of S6 range from 2 to 60 μm. S6 peaks are narrower and

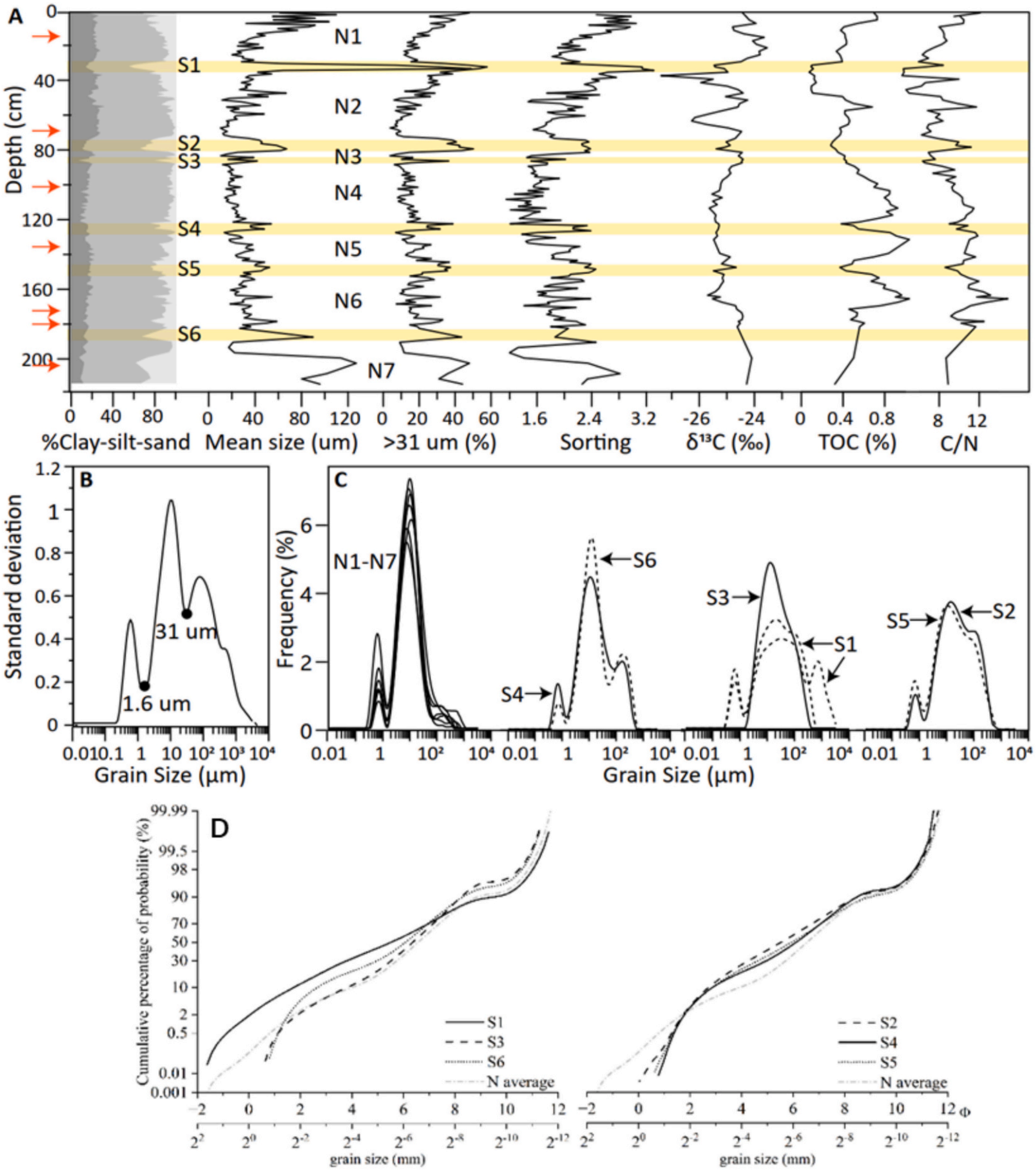

Fig. 3. A: Results of grain size composition and bulk organic carbon isotopic analyses. Sand layers (S1–6) are highlighted with yellow colour, and the red arrows are sampling depths the AMS dates. B: Results of the sensitive grain size components of Core K5. C: Grain size frequency distribution curves of the normal layers (N1–7) and sandy layers. D: Accumulative grain size frequency distribution curves of the N and S layers. (For interpretation of the references to colour in this figure legend, the reader is referred to the web version of this article.)

correspond to higher frequencies (∼6 %), compared to S4 (∼5 %).

These differences are also apparent in the cumulative grain size frequency distribution curves (Fig. 3D). The N-layers are characterized by a gently inclined curve, indicating a wide grain-size distribution with a large proportion of fine particles, which is typical of a low-energy depositional environment. In contrast, the S-layers generally present a steep, three-stage trend, reflecting deposition under strong hydrodynamic conditions with efficient sorting. Specifically, S1 contains a distinct coarse component, suggesting the rapid settling of coarser particles due to a strong, instantaneous flow or the input of near-source debris; the curve for S3 is the steepest and most concentrated. It has the largest proportion of saltation components and the narrowest particle distribution, indicating the most efficient sorting under stable, high-energy conditions; in contrast, the curve for S6 shows the poorest sorting, suggesting weaker hydrodynamics and the potential influence of multi-source mixing; the curves for S2, S4, and S5 are similar to each other, with high particle concentration and good sorting, indicating deposition under strong and relatively stable hydrodynamic conditions. S1 contains a distinct coarse component, suggesting the rapid settling of coarser particles due to a strong, instantaneous flow or the input of near-source debris; the curve for S3 is the steepest and most concentrated. It has the largest proportion of siltation components and the narrowest particle distribution, indicating the most efficient sorting under stable, high-energy conditions; in contrast, the curve for S6 shows the poorest sorting, suggesting weaker hydrodynamics and the potential influence of multi-source mixing; the curves for S2, S4, and S5 are similar to each other, with high particle concentration and good sorting, indicating deposition under strong and relatively stable hydrodynamic conditions.

4.3. *Geochemical characteristics*

4.3.1. *Bulk organic carbon isotopic signature*

The carbon isotopic composition of Core K5 is presented in Fig. 3A. The overall δ^{13}C values range from −27.39 ‰ to −23.54 ‰, with an average of −24.94 ‰. Total Organic Carbon (TOC) ranges from 0.07 % to 1.04 %, averaging 0.53 %, while the C/N ratios range from 4.29 to 14.87, with an average of 9.18.

For the fine-grained N layers, TOC content ranges from 0.09 % to 1.04 % and averages 0.56 %. Their corresponding δ^{13}C values vary between −25.71 ‰ and − 23.54 ‰, with an average of −24.74 ‰. The C/N ratios in these layers fall between 4.68 and 12.72, averaging 9.28. Within the normal sedimentation intervals, the sediments reveal further details based on their distinct geochemical signatures:

Specifically, Layers N1, N4, and N7 are characterized by relatively high average TOC at 0.53 %, within a range of 0.32 % to 0.93 %. Its δ^{13}C values average −24.56 ‰, varying from −25.64 ‰ to −23.54 ‰. The C/N ratios average 9.28 and range from 5.92 to 12.72.

Layers N2 and N3 exhibit significantly lower average TOC at 0.35 %, ranging from 0.09 % to 0.68 %. Its average δ^{13}C value is similar to the first cluster at −24.89 ‰, ranging from −27.39 ‰ to −24.24 ‰, but it possesses lower average C/N ratios of 7.24, with values between 4.29 and 11.73.

Layers N5 and N6 show a high average TOC of 0.79 %, ranging from 0.46 % to 1.04 %, and the highest average C/N ratio among N layers at 11.30, with values between 9.16 and 14.87. The average δ^{13}C for this cluster is slightly more negative at −25.16 ‰, ranging from −25.70 ‰ to −24.42 ‰.

For the coarse-grained S layers, their TOC content ranges from 0.07 % to 0.61 %, with an average of 0.38 %. The δ^{13}C values in S layers span from −25.49 ‰ to −24.41 ‰ and average − 24.93 ‰, slightly more negative on average than N layers. S layer C/N ratios vary widely from 4.41 to 12.49, averaging 8.83.

layers S1 and S3 show the lowest average TOC among S layers at 0.26 %, ranging from 0.07 % to 0.43 %. Its average δ^{13}C is −24.84 ‰, within a range of −25.46 ‰ to −24.41 ‰, and it possesses the lowest average C/N ratio at 6.48, with values between 4.41 and 8.41. Carbon isotope composition is within the range of marine-organic matter.

Layers S2, S4, and S5 are characterized by a higher average TOC of 0.40 %, ranging from 0.28 % to 0.55 %. The average δ^{13}C value for this cluster is −25.14 ‰, with values between −25.49 ‰ and − 24.66 ‰, and the average C/N ratio is higher at 9.71, ranging from 7.82 to 11.20. The notably high TOC and C/N in layers S4 and S5 might suggest these floods transported substantial amounts of freshwater plankton and terrestrial vascular plant debris.

Layer S6 exhibits a high average TOC at 0.54 %, ranging from 0.47 % to 0.61 %, and a high average C/N ratio of 10.84, with values between 9.85 and 12.49. Its average δ^{13}C value is the least negative among S layers at −24.52 ‰, ranging from −24.59 ‰ to −24.45 ‰. These characteristics suggest the flood event depositing S6 carried predominantly terrestrial plant material.

4.3.2. *Results of MCMC-based endmember modelling*

As shown in Fig. 4A, the N-layers (N1–N7) generally exhibit a balanced mixture of the five endmembers, with contributions from Soil, C3 plants, and Freshwater Particulate Organic Matter (POM) fluctuating between 18 and 28 %, and a slightly lower contribution from C4 plants (9–16 %). Layer N3 is a notable exception and a clear outlier, with significantly higher contributions from Marine POM (41.5 %) and Freshwater POM (33.5 %) compared to the other N-layers. To avoid having this outlier skew the results, N3 was excluded from the calculation of the average N-layer composition used for subsequent comparisons (Fig. 4B).

After excluding N3, the N- layer average (Soil 24.5 %, C4 13.5 %, C3 23.9 %, Freshwater 21.1 %, Marine 16.9 %) serves as a baseline to highlight the distinct provenances of the S-layers (Table 2). Layer S3, for instance, is strongly marine-dominated, with marine POM contributing 32.1 %, a typical signal of a strong storm surge. Layer S1 is characterized by a high proportion of freshwater POM (27.5 %), which, combined with a higher-than-average marine input, suggests a significant influx of riverine organic matter during a storm event. The remaining layers show a stronger terrestrial influence. Layers S2, S4, and S5 have higher contributions from terrestrial and freshwater plants and lower marine input, indicating a depositional environment dominated by terrestrial floodwaters. Similarly, Layer S6 is dominated by terrigenous sediments, highlighting the control of flood-driven surface runoff.

4.3.3. *Elemental composition feature*

The downcore distributions of selected major and trace elements and key elemental ratios are presented in Fig. 5. Within the N layers, most elemental concentrations show relatively stable trends with only gentle fluctuations. Specifically, proxies typically associated with marine influence, such as Br and Sr concentrations and the Br/Ti and Br/Al ratios, are found at consistently low values. Similarly, terrigenous elements like Si and Ti, and the K/Ti ratio, also remain at relatively low levels.

In contrast, the S layers are marked by significant and sharp excursions (peaks) in multiple indicators (Fig. 5). Most notably, the Br/Ti and Br/Al ratios display prominent peaks in all S layers. These peaks in marine-proxy ratios coincide with clear increases in Br, Sr, Si, and Ti concentrations. Conversely, the concentrations of other terrestrial elements, such as Al, K, and Fe, sometimes show a relative decrease within these same intervals.

5. Discussions

5.1. *Geochemical signature of compound flooding induced by typhoons*

Based on an integrated analysis of grain size, bulk organic δ^{13}C and C/N ratios, and major and trace elements (Fig. 6A-C), this study identified at least six major overwash deposits. In stark contrast to the low-energy background sediments, most of these overwash deposits are composed of multi-source material, including terrestrial, freshwater, and marine matter, with one source typically being dominant (Table 2).

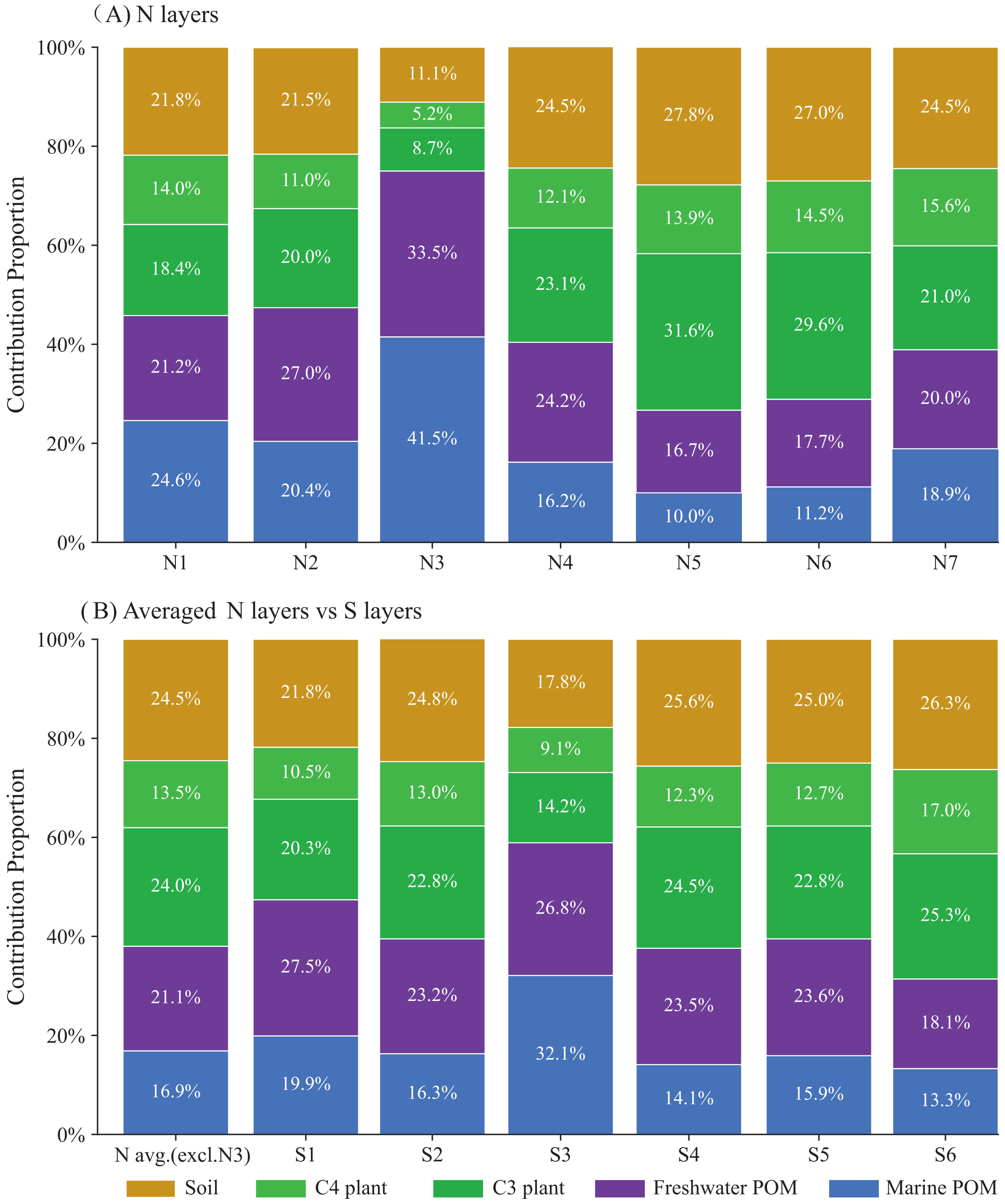

Fig. 4. A. The contribution proportion of endmembers of samples in each layer; B. Comparison of end-member contributions between N layers (exclude N3) and S layers.

Crucially, the proportional contribution from these sources varies significantly between these event layers, and this diverse mixture holds the key to revealing the specific nature of each event.

Our study area, the Zhangjiang Estuary, typically represents a low-energy depositional environment under normal hydrodynamic conditions, characterized by sediments predominantly composed of fine-grained silt and clay delivered by fluvial and modified by tidal processes (Dalrymple and Choi, 2007; Gao et al., 2021). During compound flood events, however, this area is directly subjected to both fluvial floods, originating from heavy rainfall in the upper catchment, and the incursion of marine storm surges (Chan et al., 2024; Green et al., 2025).

Layers S1 and S3 are identified as compound floods with significant marine influence (Fig. 6, Table 2). Layer S3 is a prime example of a storm-surge dominated event, with well-sorted, high-energy deposits and dominant marine signatures from MCMC and elemental analyses. In contrast, Layer S1 also shows strong marine signals but its dominant organic source is freshwater POM, highlighting a complex interplay of forces.

Conversely, Layers S2, S4, S5, and S6 are interpreted as fluvial-flood dominated events (Fig. 6, Table 2). The oldest event, S6, exemplifies this category, marked by poor grain sorting and dominant terrigenous sources confirmed by MCMC modelling and organic isotopes. Layers S2, S4, and S5 similarly show a clear dominance of terrestrial and freshwater sources in their MCMC results. Although marine elemental peaks confirm the compound nature of all these events, the integrated proxy evidence establishes fluvial processes as the primary driver.

This detailed sedimentological evidence naturally leads to the question of the driving mechanisms. In this subtropical region, typhoons stand out as the most plausible drivers capable of concurrently generating the intense storm surges and large-scale fluvial floods required to

Table 2
Justification of sediment provenance of sandy layers.

Sandy layers	Number of sources based on grain size	Organic sources based on C/N and $\delta^{13}C$	Dominant sources based on MCMC modelling	Organic sources based on element contents	Possible events
S1	2–3	Marine plankton	Freshwater POM	Marine	Storm surge and flooding
S2	2	Freshwater plankton	Soil, freshwater POM and C3 plants	Terrestrial and marine	Flooding and storm surge
S3	1	Marine plankton	Marine POM	Marine and terrestrial	Storm surge and flooding
S4	3	Freshwater plankton	Soil, C3 plants and freshwater POM	Terrestrial	Fluvial/pluvial flooding
S5	2	Freshwater plankton	Soil, freshwater POM and C3 plants	Terrestrial	Fluvial/pluvial flooding
S6	3	Terrestrial plants	Soil and C3 plants	Marine and terrestrial	Flooding and storm surge

form compound floods (Yin et al., 2010). The uniqueness of a typhoon lies in its dual impact: its low-pressure cell and violent winds drive destructive storm surges, while its torrential rainfall generates massive floods (Wahl et al., 2015). This dual action perfectly explains the high-energy, mixed-source sedimentary characteristics observed in our sandy depositional layers. This "typhoon-driven" interpretation is further corroborated by regional paleo-disaster records. As shown in Fig. 7A, the timing of the six major compound flood events identified in this study shows close correspondence with periods of high paleo-typhoon activity reconstructed in other studies from Southern China, such as those from the northern South China Sea, eastern Hainan Island, and the Nansha Islands (Shi and Yu, 2007; Zhou et al., 2019; Li et al., 2021). Crucially, when our findings are compared with high-resolution terrestrial records from neighboring regions, the history of Holocene megafloods in the nearby Pearl River basin closely matches our reconstruction (Chen et al., 2023). The synchronicity of our major fluvial-dominated events S6 (3830–3800 cal. yr BP) and S2 (1190–1020 cal. yr BP) with the Pearl River's most intense floods, FL3 (4421–4151 cal. yr BP) and FL7 (1172–782 cal. yr BP) respectively, indicates they were triggered by a shared, large-scale meteorological event that generated extreme precipitation across the broader southern China region. This regional coherence provides strong external evidence linking our local compound flood events to broader typhoon activity, and it reinforces our conclusion based on the sedimentological evidence, while also ruling out less likely causes such as tsunamis (Li et al., 2021).

Moreover, spectral analysis of $\delta^{13}C$ and sensitive grain-size fractions was conducted to investigate the frequency of typhoon-related disasters. Three significant cycles were identified: 739 years, 649 years, and 397 years (Fig. 8), all surpassing the 99 % significance threshold. The cycle derived from spectral analysis of $\delta^{13}C$ is approximately 700 years, while that derived from grain-size analysis is about 400–600 years. Similar cycles have been identified in other regions, such as northeastern China, with a 590-year cycle in peat cellulose records (Hong et al., 2000) and around a 500-year cycle in pollen records from Lake Marl (Xu et al., 2019). The Late Holocene cycle of strong typhoon occurrences in the Zhangjiang Estuary is consistent with these findings, reinforcing the cyclical nature of typhoon activity in the region.

5.2. Implications for future subtropical coastal compound floods under the background of global climate change

Periods of reduced solar irradiance are associated with increased temperature and pressure differentials between land and ocean, which intensify convective activity and favor the formation of strong tropical cyclones (Xiao et al., 2006; Zhang et al., 2017). In our study, phases of high typhoon frequency inferred from sedimentary records coincide with intervals of low solar activity (Fig. 6D), supporting the hypothesis that solar forcing plays a key role in driving late Holocene typhoon

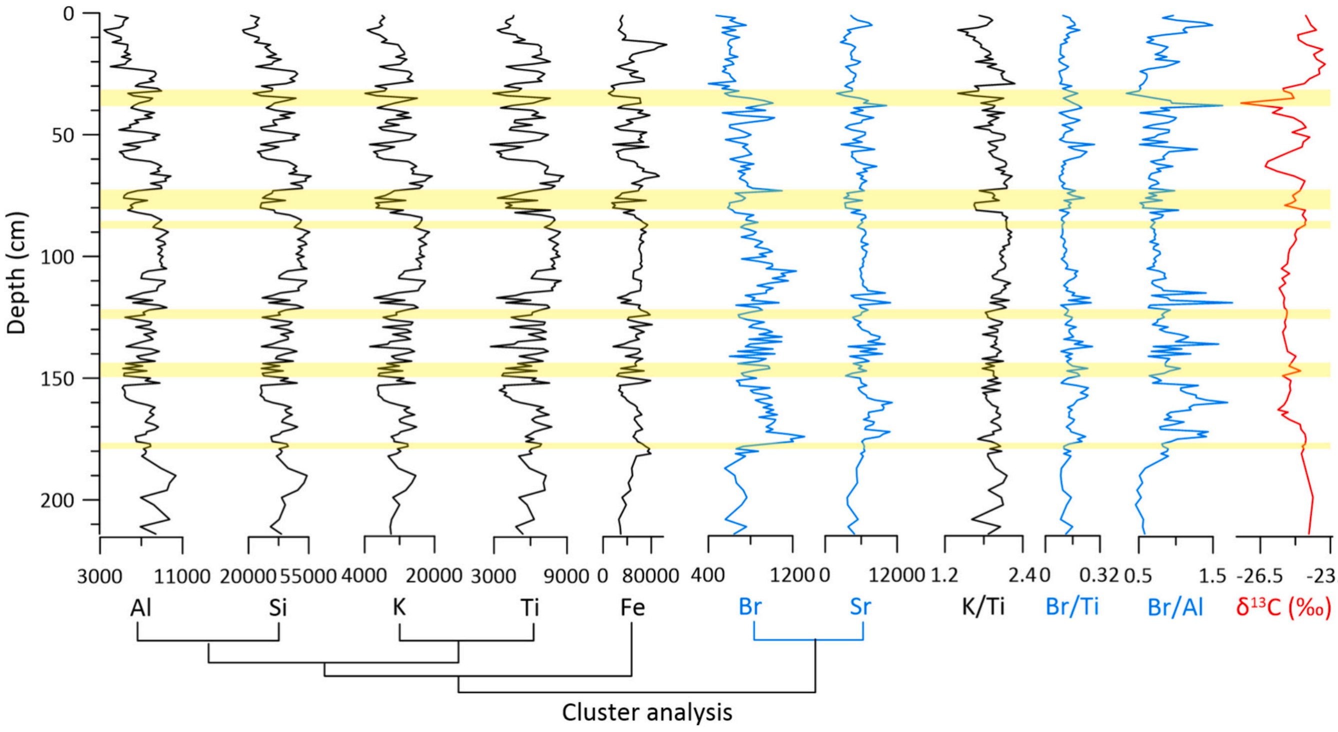

Fig. 5. Comparison of the intensity of major and trace elements in core K5 with the stable carbon isotope curve.

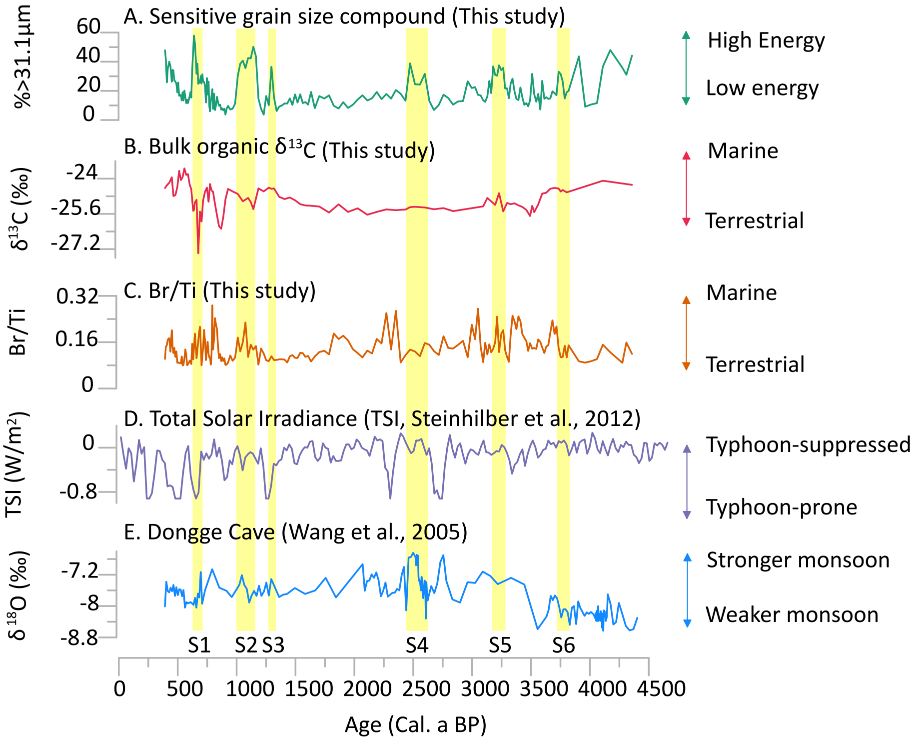

Fig. 6. Proxies of coastal hazard at Zhangjiang Estuary since the Late Holocene. Shaded events are identified six major palaeo compound flooding events (this study).

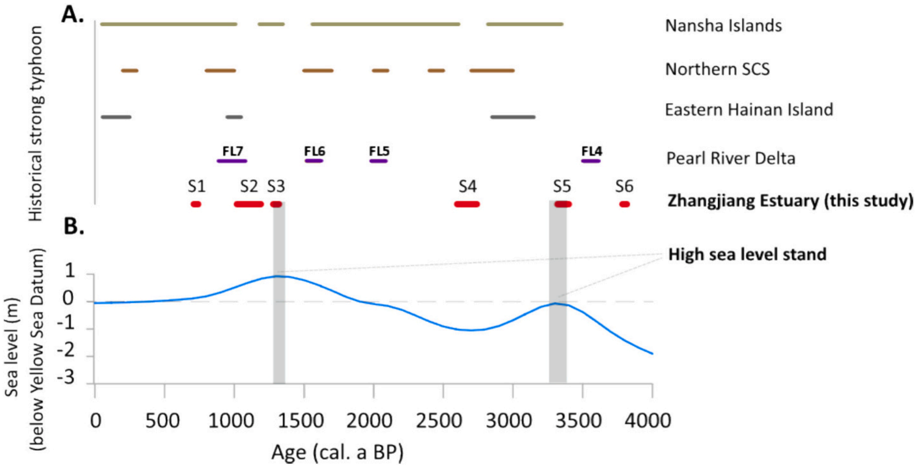

Fig. 7. A. Late Holocene Disaster History in Fujian Province (Nansha Islands: (Shi and Yu, 2007); Northern SCS: (Li et al., 2021); Eastern Hainan Island: (Zhou et al., 2019); Pearl River Delta (Chen et al., 2023); B. Late Holocene sea level history in southern Fujian Province (integrated from Yu et al., 2023).

variability (Solanki et al., 2013; Yeo et al., 2014). The comparison with Dongge Cave δ^{18}O records (Fig. 6E), a widely used monsoon proxy, reveals coherent variability during periods of frequent compound flood events, indicating that East Asian summer monsoon intensity also followed centennial-scale solar cycles (Liu et al., 2012). These findings support a coupled response of the East Asian monsoon–typhoon system to solar forcing over the late Holocene.

Moreover, our results indicate that two prominent periods of increased compound flood frequency (~3 ka BP and ~ 1 ka BP) coincide with secondary peaks in regional sea level (Yu et al., 2023) (Fig. 7B). Elevated sea levels likely raised the groundwater table and increased baseline water levels in estuarine settings, creating favorable hydrological conditions for the superposition of heavy rainfall, storm surges, and high tides. This suggests that centennial-scale sea-level variability may act as a secondary modulator of compound flood events, enhancing their magnitude during periods of higher mean sea level. Moreover, sea level change at the coastal plain area has been significantly enhanced by land deformation as a result of both monsoon-induced seasonal sea level changes and anthropogenic activities (Huang and Yu, 2023; Yu et al., 2024a, 2024b).

Under the impact of global warming, both frequency and intensity of tropical cyclones worldwide have increased significantly. For example, in the past 122 years, the frequency of tropical cyclones in the Bay of Bengal, northern Indian Ocean, in November has tripled (McCabe et al., 2001; Singh et al., 2001). From 1959 to 1997, the storm intensity in the northern hemisphere also showed an increasing trend. All the observations have suggested the possibility of more destructive extreme compound flood events in the region in the future (Krishna, 2009; Chou et al., 2020; Lu et al., 2023), which enhances the urgency for getting better knowledge of compound floods toward a safer coast.

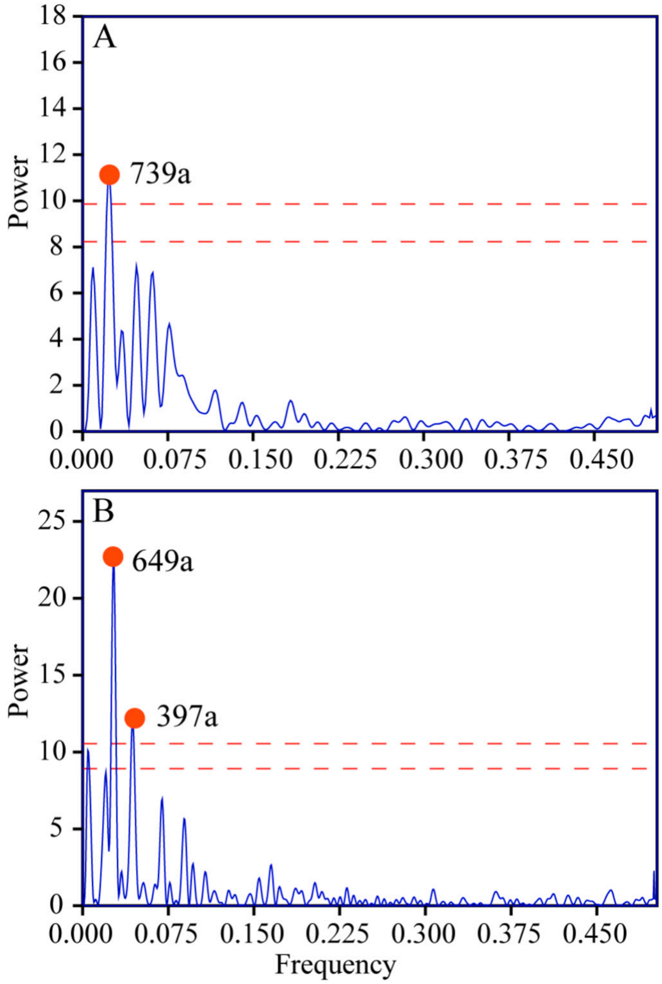

Fig. 8. Spectral analysis of Core K5. A: Results based on the $\delta^{13}C$ value; B: Results based on proportion of grain fraction >31.1 μm. Dash lines show significance levels of 99 % and 95 % respectively.

6. Conclusions

Aiming to gain a better understand on subtropical compound floods, this study was conducted at the Zhangjiang Estuary, southern China. This study demonstrated a comprehensive methodological approach for distinguishing sedimentary features of compound floods, reconstructed the history of coastal compound flooding events during the late Holocene, and discussed the driving role of subtropical typhoons. The main conclusions from this study are:

1. Deposits formed under normal weather conditions are primarily composed of silts (50–75 %), while sandy deposits are characterized by higher-than-normal sand content (25–50 %).
2. Sandy sediments exhibit a multi-source origin, incorporating both marine/estuarine and terrestrial/fluvial sources. This characteristic is indicative of compound floods driven by both fluvial floods and storm surges.
3. Typhoons, characterized by strong rainfall-driven floods and wind-driven storm surges, are identified as the primary driving mechanism for compound floods in this region. This conclusion is further supported by the observed recurrence period of 400–700 years, which aligns with periods of intense typhoon activity in the region.
4. The recurrence interval of compound floods correlates with intense typhoon activity, linking coastal archives to solar forcing. This study suggests that future climate change and centennial-scale sea-level variability jointly likely increasing the frequency and intensity of subtropical compound floods.

These findings are essential for enhancing our understanding of past coastal flood dynamics and provide critical data for coastal risk assessment and management strategy development in subtropical areas for a safer coast.

CRediT authorship contribution statement

Muyi Zhang: Writing – review & editing, Writing – original draft, Visualization, Methodology. **Zixian Zhuang:** Writing – original draft, Visualization, Methodology, Investigation. **Zhaoquan Huang:** Writing – review & editing, Visualization, Software, Funding acquisition, Conceptualization. **Nannan Li:** Writing – review & editing, Validation, Methodology. **Jianghui Li:** Writing – review & editing, Funding acquisition, Conceptualization. **Shengtao Liu:** Writing – review & editing, Methodology, Investigation. **Fengling Yu:** Writing – review & editing, Writing – original draft, Resources, Project administration, Methodology, Investigation, Funding acquisition, Data curation, Conceptualization.

Declaration of competing interest

The authors declare that the research was conducted in the absence of any commercial or financial relationships that could be construed as a potential conflict of interest.

Acknowledgments

This work was supported by the Archaeological Talent Promotion Program of China (2024-269): the 2024 Shandong Weihai Underwater Archaeological Survey program by National Center for Archaeology of China (No. 20243160A0965), Central guidance for local scientific and technological development funding projects of Fujian Province (Grant No. 2022L3015), China and the National Natural Science Foundation of China (Grant No. 41706039), and MEL Internal Program of Xiamen University under contract No. MELRI2303. We are sincerely grateful for the support provided by Liangrong Zou, Tian Xia, Nengwang Chen and Zhishan Fang during the field work and data acquisition. We would also like to extend our special thanks to Prof. Yongqiang Zong from Guangzhou Institute of Geography, China, for his insightful comments on this manuscript. Finally, we are grateful to the two anonymous reviewers for their constructive feedback, which significantly improved the quality of this paper.

Data availability

The authors confirm that all data necessary for supporting the scientific findings of this paper have been provided.

References

Ali, J., Wahl, T., Morim, J., et al., 2025. Multivariate compound events drive historical floods and associated losses along the U.S. East and Gulf coasts. npj Nat. Hazards 2, 19.

Aziz, F., Wang, X., Mahmood, M.Q., et al., 2024. Coastal urban flood risk management: challenges and opportunities – a systematic review. J. Hydrol. 645, 132271.

Benito, G., Ballesteros-Cánovas, J.A., Díez-Herrero, A., 2023. Chapter 2 - Paleoflood hydrology: reconstructing rare events and extreme flood discharges. In: Shroder, J. F., Paron, P., Di Baldassarre, G. (Eds.), Hydro-Meteorological Hazards, Risks, and Disasters, Second edition. Elsevier, Boston, pp. 33–83.

Boulay, S., Colin, C., Trentesaux, A., et al., 2023. Mineralogy and sedimentology of Pleistocene sediment in the South China Sea (ODP Site 1144). Proc. Ocean Drill. Program Part B Sci. Results 184 (211), 1–21.

Chan, F.K.S., Lu, X., Li, J., et al., 2024. Compound flood effects, challenges and solutions: Lessons toward climate-resilient Chinese coastal cities. Ocean Coast. Manag. 249, 107015.

Chen, C., Zheng, Y., Zheng, Z., et al., 2023. Holocene millennial-scale megaflood events point to ENSO-driven extreme climate changes. Sci. China Earth Sci. 66, 2530–2545.

Chiverrell, R.C., Sear, D.A., Warburton, J., et al., 2019. Using lake sediment archives to improve understanding of flood magnitude and frequency: recent extreme flooding in Northwest UK. Earth Surf. Process. Landf. 44, 2366–2376.

Chou, J., Dong, W., Tu, G., et al., 2020. Spatiotemporal distribution of landing tropical cyclones and disaster impact analysis in coastal China during 1990–2016. Phys. Chem. Earth Parts A/B/C 115, 102830.

Dalrymple, R.W., Choi, K., 2007. Morphologic and facies trends through the fluvial–marine transition in tide-dominated depositional systems: A schematic framework for environmental and sequence-stratigraphic interpretation. Earth Sci. Rev. 81, 135–174.

Fang, J., Liu, W., Yang, S., et al., 2017. Spatial-temporal changes of coastal and marine disasters risks and impacts in mainland China. Ocean Coast. Manag. 139, 125–140.

Fu, S., Xiong, H., Zong, Y., et al., 2020. Reasons for the low sedimentation and slow progradation in the Pearl River delta, southern China, during the middle Holocene. Mar. Geol. 423, 106133.

Fujian Provincial Marine Disaster Bulletin, 2023. Fujian Provincial Department of Ocean and Fisheries. https://hyyyj.fujian.gov.cn/xxgk/tzgg/202409/t20240902_6510048.htm (Lastest accessed on October 20, 2025).

Gao, C., Yu, F., Chen, J., et al., 2021. Anthropogenic impact on the organic carbon sources, transport and distribution in a subtropical semi-enclosed bay. Sci. Total Environ. 767, 145047.

Gelman, A., Carlin, J.B., Stern, H.S., et al., 2013. Bayesian Data Analysis, Third Edition.

Green, J., Haigh, I.D., Quinn, N., et al., 2025. Review article: A comprehensive review of compound flooding literature with a focus on coastal and estuarine regions. Nat. Hazards Earth Syst. Sci. 25 (2), 747–816.

Hammer, O., Harper, D.A., Ryan, P.D., 2001. Palaeontological statistics software package for education and data analysis. Palaeontol. Electron. 4 (1), 1–9.

Haslett, J., Parnell, A., 2008. A simple monotone process with application to radiocarbon-dated depth chronologies. J. R. Stat. Soc.: Ser. C: Appl. Stat. 57 (4), 399–418.

He, W., Zhong, J., Sun, N., 2023. Discovery and significance of tempestites and storm deposits in the Qingshankou Formation of the Gulong Sag, northeastern China. Front. Earth Sci. 10, 999135.

Heegaard, E., Birks, H.J.B., Telford, R.J., 2005. Relationships between calibrated ages and depth in stratigraphical sequences: an estimation procedure by mixed-effect regression. The Holocene 15 (4), 612–618.

Hong, Y., Jiang, H., Liu, T., et al., 2000. Response of climate to solar forcing recorded in a 6000-yearδ^{18}O time-series of Chinese peat cellulose. The Holocene 10 (1), 1–7.

Huang, Z., Yu, F., 2023. InSAR-derived surface deformation of Chaoshan Plain, China: Exploring the role of human activities in the evolution of coastal landscapes. Geomorphology 426, 108606.

Khan, N.S., Horton, B.P., McKee, K.L., et al., 2013. Tracking sedimentation from the historic A.D. 2011 Mississippi River flood in the deltaic wetlands of Louisiana, USA. Geology 41 (4), 391–394.

Krishna, M.K., 2009. Intensifying tropical cyclones over the North Indian Ocean during summer monsoon—Global warming. Glob. Planet. Chang. 65 (1), 12–16.

Lee, Y., Yu, F., Switzer, A.D., et al., 2012. Developing a historical typhoon database for the southeastern Chinese coastal provinces, 1951–2010. Proc. Annu. Int. Conf. Geol. Earth Sci. 8–12.

Li, D., Xu, Y., Li, Y., et al., 2018. Sedimentary records of human activity and natural environmental evolution in sensitive ecosystems: A case study of a coral nature reserve in Dongshan Bay and a mangrove forest nature reserve in Zhangjiang River estuary, Southeast China. Org. Geochem. 121, 22–35.

Li, P., Li, M., Gan, H., et al., 2021. A preliminary study on sediment records of possible typhoon in the northern South China Sea during the past 6500 years. The Holocene 31 (7), 1221–1228.

Liu, H., Lin, Z., Qi, X., et al., 2012. Possible link between Holocene East Asian monsoon and solar activity obtained from the EMD method. Nonlin. Process. Geophys. 19 (4), 421–430.

Lu, J., Li, A., Zhang, J., et al., 2023. Sedimentary record off the Yangtze River estuary and its response to typhoons and human activities over the past 70 years. Reg. Stud. Mar. Sci. 65, 103074.

McCabe, G.J., Clark, M.P., Serreze, M.C., 2001. Trends in Northern Hemisphere surface cyclone frequency and intensity. J. Clim. 14 (12), 2763–2768.

Parnell, A.C., Haslett, J., Allen, J.R.M., et al., 2008. A flexible approach to assessing synchroneity of past events using Bayesian reconstructions of sedimentation history. Quat. Sci. Rev. 27 (19), 1872–1885.

Peng, F., Prins, M.A., Kasse, C., et al., 2019. An improved method for paleoflood reconstruction and flooding phase identification, applied to the Meuse River in the Netherlands. Glob. Planet. Chang. 177, 213–224.

Phillips, D.L., Gregg, J.W., 2003. Source partitioning using stable isotopes: coping with too many sources. Oecologia 136 (2), 261–269.

Razum, I., Miko, S., Ilijanić, N., et al., 2020. A compositional approach to the reconstruction of geochemical processes involved in the evolution of Holocene marine flooded coastal karst basins (Mljet Island, Croatia). Appl. Geochem. 116, 104574.

Reimer, P.J., Bard, E., Bayliss, A., et al., 2013. IntCal13 and Marine13 radiocarbon age calibration curves 0–50,000 years cal BP. Radiocarbon 55 (4), 1869–1887.

Salvatier, J., Wiecki, T.V., Fonnesbeck, C., 2016. Probabilistic programming in Python using PyMC3. PeerJ Comput. Sci. 2, e55.

Shi, Q., Yu, K., 2007. Storm event records from the lagoon sediment on Yongshu Reef of the Nansha Islands since late Holocene. Trop. Geogr. 27 (1), 1–5 (In Chinese with English abstract).

Shepard, F., 1954. Nomenclature based on sand-silt-clay ratios. J. Sediment. Res. 24 (3), 151–158.

Shi, X., Shengfa, L., Shuqin, Q., et al., 2015. Geochemical characteristics, controlling factor and record of paleoclimate in sediments from Eastern China Seas. Bull. Mineral. Petrol. Geochem. 5, 885–894.

Singh, O., Khan, T.M.A., Rahman, M.S., 2001. Has the frequency of intense tropical cyclones increased in the North Indian Ocean? Curr. Sci. 80 (4), 575–580.

Smrkulj, N., Miko, S., Razum, I., et al., 2025. Holocene paleoenvironmental changes recorded in the sediments of the karst Krka River estuary (eastern Adriatic coast, Croatia). Catena 251, 108811.

Solanki, S., Krivova, N., Haigh, J., 2013. Solar irradiance variability and climate. Annu. Rev. Astron. Astr. 51, 311–351.

Switzer, A.D., Yu, F.L., Gouramanis, C., et al., 2014. Integrating different records to assess coastal hazards at multi-century timescales. J. Coast. Res. 70, 723–728.

Szcześniak, M., Kokociński, M., Jagodziński, R., et al., 2023. Late Holocene Vistula River floods recorded in grain size distributions and diatom assemblages of marine sediments of the Gulf of Gdańsk (Baltic Sea). Palaeogeogr. Palaeoclimatol. Palaeoecol. 617, 111499.

Turner, R.E., Baustian, J.J., Swenson, E.M., et al., 2006. Wetland Sedimentation from Hurricanes Katrina and Rita. Science 314 (5798), 449–452.

Wahl, T., Jain, S., Bender, J., et al., 2015. Increasing risk of compound flooding from storm surge and rainfall for major US cities. Nat. Clim. Chang. 5 (12), 1093–1097.

Wang, Z., Chen, Y., Zeng, Z., et al., 2024. Compound effects in complex estuary-ocean interaction region under various combination patterns of storm surge and fluvial floods. Urban Clim. 58, 102186.

Wei, S., 2019. Research on identification of major ecological risk sources in Dongshan Bay. J. Fish. Res. 41 (2), 140–148.

Wei, B., Hou, Z., Chen, S., et al., 2019. Grain-size characteristics of Dayeze lake sediments in the lower reach of Yellow River and their environmental implications. Mar. Geol. Quat. Geol. 39 (3), 151–161.

Wei, J., Jin, J., Zuo, X., et al., 2023. Cultural exchange indicated by geochemical characteristic of pottery from neolithic island type sites in Fujian Province, China. Sci. Geogr. Sin. 43 (06), 1101–1112.

Xiao, S., Li, A., Liu, J., et al., 2006. Coherence between solar activity and the East Asian winter monsoon variability in the past 8000 years from Yangtze River-derived mud in the East China Sea. Palaeogeogr. Palaeoclimatol. Palaeoecol. 237 (2–4), 293–304.

Xu, D., Lu, H., Chu, G., et al., 2019. Synchronous 500-year oscillations of monsoon climate and human activity in Northeast Asia. Nat. Commun. 10, 4105.

Yang, J., Liu, Z., Yin, J., et al., 2023. Paleoflood Reconstruction in the lower Yellow River Floodplain (China) based on Sediment Grain size and Chemical Composition. Water 15 (24), 4268.

Yeo, k., Krivova, N., Solanki, S., 2014. Solar Cycle Variation in Solar Irradiance. Space Sci. Rev. 186, 137–167.

Yin, Y., Gemmer, M., Luo, Y., et al., 2010. Tropical cyclones and heavy rainfall in Fujian Province, China. Quat. Int. 226 (1), 122–128.

Yu, F., Switzer, A.D., 2014. Using geology as a tool for assessing coastal risk in Asia. In: Tang, D.L., Sui, G. (Eds.), Typhoon Impact and Crisis Management. Springer Berlin Heidelberg, Berlin, Heidelberg, pp. 539–552.

Yu, F., Zong, Y., Lloyd, J.M., et al., 2010. Bulk organic δ13C and C/N as indicators for sediment sources in the Pearl River delta and estuary, southern China. Estuar. Coast. Shelf Sci. 87 (4), 618–630.

Yu, F., Adam, D.S., Zheng, Z., et al., 2013. Sedimentary records as an indicator for palaeo typhoon hazards from the Rongjiang River Delta, Chaoshan Plain, southern China. Quat. Sci. 33 (6), 1171–1182 (In Chinese with English abstract).

Yu, F., Li, N., Tian, G., et al., 2023. A re-evaluation of Holocene relative sea-level change along the Fujian coast, southeastern China. Palaeogeogr. Palaeoclimatol. Palaeoecol. 622, 111577.

Yu, F., Huang, Z., Zhou, L., et al., 2024a. Multi-temporal InSAR evidence of Non-tidal Ocean Loading Effects from Chaoshan Coastal Plain, China. Int. J. Appl. Earth Obs. Geoinf. 132, 104031.

Yu, F., Switzer, A.D., Zheng, Z., et al., 2024b. Holocene geomorphological evolution of a sediment-starved coastal embayment in response to sea level change: Insights from the Qing’ao Embayment, southern China. Palaeogeogr. Palaeoclimatol. Palaeoecol. 633, 111895.

Yu, F., Ma, J., Huang, Z., et al., 2025. Sedimentary organic matters within the subtropical mountainous river-estuary-bay continuum: provenances, fates and implications. Int. J. Sediment Res. https://doi.org/10.1016/j.ijsrc.2025.07.005. In Press.

Zemunik, P., Denamiel, C., Šepić, J., et al., 2022. High-frequency Sea-level analysis: Global distributions. Glob. Planet. Chang. 210, 103775.

Zhang, Z., Huang, W., Chen, J., et al., 2017. Multi-time scale analysis of East Asian summer monsoon and its possible mechanism during Holocene. Quat. Sci. 37 (3), 498–509 (In Chinese with English abstract).

Zhou, L., Gao, S., Jia, J., et al., 2019. Extracting historic cyclone data from coastal dune deposits in eastern Hainan Island, China. Sediment. Geol. 392, 105524.

Zhou, L., Gao, S., Jia, J., et al., 2021. Paleo-Typhoon events as Indicated by Coral Reef Boulder Deposits on the Southern Coast of Hainan Island, China. Front. Mar. Sci. 8, 746773.

Zscheischler, J., Westra, S., van den Hurk, B.J.J.M., et al., 2018. Future climate risk from compound events. Nat. Clim. Chang. 8 (6), 469–477.